



## Full Text View

[Volume 30, Issue 9 \(September 2000\)](#)

### Journal of Physical Oceanography

Article: pp. 2391–2403 | [Abstract](#) | [PDF \(343K\)](#)

# Buoyancy- and Wind-Driven Circulation in an Extended Model of Potential Vorticity Homogenization

Shigeto Nishino<sup>+</sup> and Shoshiro Minobe<sup>+</sup>

*Division of Earth and Planetary Sciences, Graduate School of Science, Hokkaido University, Japan*

(Manuscript received November 27, 1998, in final form November 19, 1999)

DOI: 10.1175/1520-0485(2000)030<2391:BAWDCI>2.0.CO;2

## ABSTRACT

An analytical model is proposed on the middepth water circulation between the surface wind-driven circulation and the deep buoyancy-driven circulation. The model consists of three and a half layers, with the second and third layers being the middepth layers. The model includes thermohaline processes by allowing diapycnal flows at interfaces between layers, in addition to the potential vorticity homogenization proposed by Rhines and Young. The velocities of diapycnal flow are calculated from the density stratification, which can be given solely by a wind-driven model as a good approximation. The divergence of diapycnal velocity causes a circulation in addition to the wind-driven circulation. Although, in pure wind-driven theories, motion was absent outside the region of homogenized potential vorticity, the present model gives significant currents there. In particular, a prominent eastward flow appears in the third layer along the southern rim of the homogeneous potential vorticity region in the second layer. The flow pattern in the present model is consistent with that estimated diagnostically from the climatological density distribution in the North Pacific. The diagnosed flow field is further supported by the oxygen distribution there.

## 1. Introduction

The ocean is driven by wind and thermohaline forcings, with different contributions at different depths. Wind forcings play the dominant role in the surface layer where the ocean circulation is explained by wind-driven theories such as the ventilated thermocline theory (Luyten et al. 1983, hereafter referred to as LPS). On the other hand, buoyancy forcings caused by thermohaline processes are dominant over the wind forcings in the deep layer where diapycnal flows, which cross density surfaces, induce a buoyancy-driven circulation (Stommel and Arons 1960a,b). For the layer sandwiched by the surface and deep layers, both the wind and buoyancy forcings may play

### Table of Contents:

- [Introduction](#)
- [Analytical model](#)
- [Results](#)
- [Discussion](#)
- [Conclusions](#)
- [REFERENCES](#)
- [TABLES](#)
- [FIGURES](#)

### Options:

- [Create Reference](#)
- [Email this Article](#)
- [Add to MyArchive](#)
- [Search AMS Glossary](#)

### Search CrossRef for:



- [Articles Citing This Article](#)



### Search Google Scholar for:


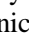
- [Shigeto Nishino](#)
- [Shoshiro Minobe](#)


important roles. This part of the ocean, which is not ventilated by the surface wind forcings and is not dominated by the buoyancy-driven circulation, is referred to as the middepth ocean in the present paper.

The influence of the surface wind forcings on the unventilated middepth ocean has been studied theoretically, with buoyancy effects being ignored. [Rhines and Young \(1982a, hereafter referred to as RY82a\)](#) proposed a model that the circulation in the middepth ocean is not driven by the direct wind forcings but induced by baroclinic instability associated with mesoscale eddies. [Rhines and Young \(1982b, hereafter referred to as RY82b\)](#) argued that the mesoscale eddies act to diffuse potential vorticity (PV) horizontally, resulting in homogenization of the PV in the region surrounded by a closed streamline. This region is referred to as a PV-homogenized region, where a resultant wind-driven gyre exists. Furthermore, [Pedlosky and Young \(1983, hereafter referred to as PY\)](#) studied the wind-driven circulation in the ventilated layer and the middepth layer, combining the theories of LPS and RY82a,b.

The wind-driven models of RY82a and PY explain the PV distribution most successfully in the subtropical North Pacific in comparison with the other oceans (e.g., [Keffer 1985](#)). In the subtropical North Pacific, the homogenized PV is observed between hundreds of meters and about 2000 m ([Talley 1988](#)). On the density surface of  $26.8\sigma_\theta$  near the depth of 500 m in the subtropical North Pacific ([Fig. 1a](#) ), PV is approximately uniform between  $20^\circ$  and  $43^\circ\text{N}$ , and exhibits sharp meridional gradients roughly south of  $20^\circ\text{N}$ . On the  $27.4\sigma_\theta$  surface near the 1000-m depth ([Fig. 1b](#) ) , the distinction between these two regions of homogeneous PV and steep PV gradients is evident, with the homogeneous region in the subtropical ocean being contracted, as predicted by the models, roughly north of  $30^\circ\text{N}$ .

Successful PV reproduction by the wind-driven models implies that the models also explain the observed density stratification in the subtropical North Pacific. [Figure 2a](#)  indicates the meridional cross section of observed density along the date line. The aforementioned PV-homogenized regions are recognized on concave density surfaces, contracting northward as the depth increases. The regions of steep meridional PV gradients correspond to regions where density surfaces are almost horizontal. These features are qualitatively well reproduced by the wind-driven model as shown in [Fig. 2b](#) .

Although the PV and density distributions in the subtropical North Pacific have been explained well by the wind-driven models for the middepth ocean, circulation patterns cannot be explained fully by the models. In the wind-driven models, a gyre circulation exists only in the PV-homogenized region, and waters cannot move outside this region. Observational studies, however, have revealed that significant water movements exist outside the PV-homogenized region. Very recently, [Reid \(1997\)](#) investigated geostrophic flow fields in the Pacific Ocean, using data from 32 high-quality expeditions from 1960 to 1992. The circulation in the subtropical North Pacific at 500 db is characterized by an anticyclonic gyre north of  $10^\circ\text{N}$ . At this depth, however, the PV-homogenized region in the subtropics appears roughly north of  $20^\circ\text{N}$  ([Fig. 1a](#) ). Thus, the flow between  $10^\circ$  and  $20^\circ\text{N}$  cannot be explained by the wind-driven models. Moreover, in [Reid's \(1997\)](#) 1000-db map, in addition to an anticyclonic gyre that is contracted north of  $30^\circ\text{N}$  in the subtropics, an eastward flow appears around  $20^\circ\text{N}$ , where the flow direction at 500 db is westward. The PV-homogenized region at this depth is restricted roughly north of  $30^\circ\text{N}$  ([Fig. 1b](#) ). As a consequence, waters are in motion south of the PV-homogenized region, with a baroclinic flow structure between the 500-db and 1000-db surfaces. Similar current patterns are found in the classical studies of [Reid \(1965\)](#), [Reid and Arthur \(1975\)](#), and [Reid and Mantyla \(1978\)](#). Furthermore, recent float observations in the western North Pacific support the existence of the eastward flow around  $20^\circ\text{N}$  at the depth of 1000 m (see Figs. 2 and 3 in [Riser 1995](#)).

In order to understand the circulation mechanism outside the PV-homogenized region, we must include other effects that were not in the models of RY82a and PY. South of the PV-homogenized region, PV contours extend almost in the zonal direction and eventually encounter the eastern boundary ([Fig. 1](#) ). Geostrophic motion along a PV contour is then prohibited by the condition of no normal-flow at the eastern boundary. To produce water movements, therefore, PV must be inputted to a water column to cross the PV contours. The eddy activities, which play an important role in the PV-homogenized region, are not likely to produce a prominent flow, such as the eastward flow around  $20^\circ\text{N}$  at the 1000-m depth in the North Pacific, as strong as the gyre flow in the homogenized region. In eddy-resolving numerical models (e.g., [Holland and Rhines 1980](#); [Holland et al. 1984](#); [Lozier and Riser 1989](#)), the strength of flows is much smaller outside the PV-homogenized region than inside the region. In addition, observations indicate that eddy kinetic energy is much smaller outside the PV-homogenized region than inside the region (e.g., [Schmitz and Holland 1982, 1986](#); [Riser 1995](#)).

Another candidate for the PV input is the divergence (convergence) of diapycnal flow that causes vertical stretching (compression) of a water column. The diapycnal flows are in a thermohaline balance such that the upward diapycnal advection of cold water balances the downward diapycnal diffusion of heat to maintain density stratification ([Munk 1966](#)). The diapycnal thermohaline balance holds over the entire interior ocean, in contrast to the effect of mesoscale eddies, which is significant in the PV-homogenized region. Therefore, the diapycnal divergence might be the primary source for the PV input outside the PV-homogenized region. The PV input due to the diapycnal divergence produces a buoyancy-driven circulation in the middepth ocean in addition to the wind-driven circulation.

The aforementioned fact that density stratification is obtained from a wind-driven model allows us to calculate an

analytical solution of the buoyancy-driven circulation. We first employ a wind-driven model to obtain density stratification. Then, we estimate diapycnal velocities based on the stratification. Finally, we can obtain the buoyancy-driven circulation caused by the divergence of diapycnal velocity. The assumption that the diapycnal velocities can be estimated from the stratification determined from a wind-driven model has been used previously (e.g., [Tziperman 1986](#); [de Szoeke 1995](#)). The purpose of the present paper is, therefore, to propose an analytical model on the middepth water circulation that includes both the wind and buoyancy forcings. The present model is useful for analyzing the circulation in the middepth of the subtropical North Pacific, where the PV and density distributions are explained very well by the PV-homogenization models as described above.

The combined effects of wind and buoyancy forcings have been examined theoretically in previous studies. Most of them used two-layer models (e.g., [Veronis 1978](#); [Luyten and Stommel 1986b](#); [Cushman-Roisin 1987](#)). Apparently, the vertical resolution of these models is too low to study the mechanism of the middepth water circulation. [Pedlosky \(1986\)](#), [Tziperman \(1986\)](#), and [de Szoeke \(1995\)](#) developed models with three or more layers, but took only the ventilated thermocline into account in their wind-driven circulation, and did not include the PV-homogenized region. The buoyancy effects combined with the PV homogenization have not been examined theoretically so far.

The present paper is organized as follows. Model formulation and parameters are described in [section 2](#), and the results are depicted in [section 3](#). Discussion of results is given in [section 4](#), and conclusions are presented in [section 5](#).

## 2. Analytical model

### a. Model formulation

In the model, the subtropical North Pacific is idealized as rectangular and divided into four vertical layers: a surface layer, an upper intermediate layer, a lower intermediate layer, and a deep layer. Only the surface layer outcrops at the sea surface, and is forced directly by wind stresses. The upper and lower intermediate layers correspond to the middepth ocean. As described in [section 1](#), the observed circulation patterns are different between 500-db and 1000-db depths (e.g., [Reid 1997](#)). Therefore, in order to take this difference into account, we divide the middepth ocean into two layers. The deep layer is assumed to be at rest with an infinite depth. The model includes only the interior region of the ocean, excluding a western boundary region. The wind forcing is given in the form of Ekman pumping at the top of the surface layer. The buoyancy forcing is taken into account by allowing diapycnal flows at the upper and lower interfaces of each layer. A schematic depiction of the model is given in [Fig. 3](#).

The wind-driven circulation and accompanying layer thicknesses are determined from a wind-driven model based on PY. Although the PY model has multiple ventilated layers, the present model has only one outcropping layer because we are interested in the circulation not in the ventilated layer but in the middepth layer. In the  $n$ th layer of the present model,  $u_n^w$  and  $\mathbf{v}_n^w$  represent zonal and meridional velocities of the wind-driven circulation, respectively, and  $h_n^w$  is the accompanying thickness. The motion in each layer is assumed to be geostrophic and hydrostatic, and the fluid satisfies continuity. At the northern boundary of the model domain, which corresponds to the boundary between the subtropical and subpolar regions, the no cross-flow condition is applied. At the eastern boundary of the model domain, the no normal-flow condition is employed. Therefore, along the northern and eastern boundaries, the layer thicknesses are constant, and are expressed as  $H_n$ . Furthermore, according to RY82b, PV is assumed to be constant within the region in motion in each intermediate layer. Consequently, the wind-driven circulation in the intermediate layer is confined to the northwestern corner of the model domain where PV is homogeneous. Outside of this PV-homogenized region, the velocity of the wind-driven circulation is zero. Detail descriptions are referred to PY.

In addition to the wind-driven circulation, diapycnal flows induce a buoyancy-driven circulation. The zonal and meridional velocities associated with the buoyancy-driven circulation are expressed as  $u_n^t$  and  $\mathbf{v}_n^t$ , respectively, and a layer thickness distortion from the thickness that is determined from the wind-driven model described above is referred to as  $h_n^t$ . The velocity of diapycnal flow is estimated from a density balance maintained by diapycnal advection and diffusion. As shown by [Tziperman \(1986\)](#), the diapycnal advective–diffusive density balance is expressed as a finite difference formula for the layer model, and the diapycnal velocity at the interface between the layers  $n$  and  $(n + 1)$ ,  $w_n^*$ , can be written as follows:

$$w_n^* = \kappa^* \frac{\Delta_{n+1}\rho/(h_{n+1}^w + h_{n+1}^t) - \Delta_n\rho/(h_n^w + h_n^t)}{\rho_{n+1} - \rho_n}, \quad (1)$$

where  $\kappa^*$  is the diffusion coefficient of diapycnal mixing,  $\rho_n$  is the density in the  $n$ th layer, and  $\Delta_n\rho$  is the density difference between the upper and lower interfaces of the  $n$ th layer. Although the density of the  $n$ th layer is given as a

constant value of  $\rho_n$ , interface densities,  $\rho_n^T$  and  $\rho_n^B$ , are defined at the top and bottom interfaces of the  $n$ th layer, respectively, and their difference gives the interface density difference,  $\Delta_n \rho \equiv \rho_n^T - \rho_n^B$ . The interface density at the bottom of the layer  $n$  is identical to the interface density at the top of the layer  $(n + 1)$ . The aforementioned good agreement in the density stratification between the observation and the wind-driven model (Fig. 2) suggests that the relation,  $h_n^w \gg h_n^t$ , holds well. In this case, (1) is approximated as

$$w_n^* = \kappa^* \frac{\Delta_{n+1} \rho / h_{n+1}^w - \Delta_n \rho / h_n^w}{\rho_{n+1} - \rho_n}. \quad (2)$$

Consequently, the diapycnal velocity is calculated from the layer thicknesses determined from the wind-driven model.

The layer thickness distortion,  $h_n^t$ , accompanied by the buoyancy-driven circulation is calculated from a PV equation. Under the relation,  $h_n^w \gg h_n^t$ , the PV equation outside the PV-homogenized region in the  $n$ th layer is expressed as

$$u_n^t \frac{\partial}{\partial x} \left( \frac{f}{h_n^w} \right) + v_n^t \frac{\partial}{\partial y} \left( \frac{f}{h_n^w} \right) = \frac{f(w_{n-1}^* - w_n^*)}{h_n^{w2}}, \quad (3)$$

$$\left. \begin{aligned} u_n^t &= -\frac{1}{f} \frac{\partial}{\partial y} \sum_{j=n}^m \gamma_j \sum_{i=1}^j h_i^t \\ v_n^t &= \frac{1}{f} \frac{\partial}{\partial x} \sum_{j=n}^m \gamma_j \sum_{i=1}^j h_i^t \end{aligned} \right\}, \quad (4)$$

where  $f$  is the Coriolis parameter,  $m$  is the number of the deepest layer in motion ( $m = 3$ ), and  $\gamma_n$  is the reduced gravity defined as  $\gamma_n = g(\rho_{n+1} - \rho_n) / \rho_n$ . In the lower intermediate layer ( $n = 3$ ), the PV equation of (3) is written as

$$-\frac{\partial}{\partial x} \left( \frac{f}{h_3^w} \right) \frac{\partial d_3^t}{\partial y} + \frac{\partial}{\partial y} \left( \frac{f}{h_3^w} \right) \frac{\partial d_3^t}{\partial x} = \frac{1}{\gamma_3} \left( \frac{f}{h_3^w} \right)^2 (w_2^* - w_3^*), \quad (5)$$

where  $d_3^t = h_1^t + h_2^t + h_3^t$  represents the total layer thickness distortions or a deviation of the bottom interface depth of the lower intermediate layer from its depth at the eastern boundary. The solution of  $d_3^t$  is obtained by integrating the right-hand side of (5) along a characteristic path, on which  $f/h_3^w$  is constant, from the eastern boundary where  $d_3^t$  is presumed to be zero. Subsequently, the velocity field of the buoyancy-driven circulation can be calculated from (4). Likewise, the buoyancy-driven circulation in the upper intermediate layer is evaluated from the distribution of the divergence of diapycnal velocity,  $w_1^* - w_2^*$ , along the characteristic path, where  $f/h_2^w$  is constant. The velocity normal to a constant PV line,  $\mathbf{v}_{n\perp}^t$ , however, can be more easily obtained from the following Sverdrup balance,


$$\mathbf{v}_{n\perp}^t \left( \frac{f}{h_n^w} \right)_{\perp} = \frac{f(w_{n-1}^* - w_n^*)}{h_n^{w2}}, \quad (6)$$

which is directly derived from (3), where  $(f/h_n^w)_{\perp}$  is the derivative of PV in the normal direction to a constant PV line.

The characteristic paths emanating from the eastern boundary do not penetrate into the PV-homogenized region. Thus, we cannot obtain the flow field of the buoyancy-driven circulation in the PV-homogenized region, but assume that the wind-driven circulation is dominant over the buoyancy-driven circulation there. In this region, if the divergence of diapycnal flow for the PV input were as large as the effect of mesoscale eddies, which acts to homogenize PV within a closed gyre circulation, the distribution of PV would be no longer homogeneous. Observational evidence of the homogeneous PV (e.g., Talley 1988; see also Fig. 1), however, suggests that the divergence of diapycnal flow for the PV input is much smaller than the homogenization agency by the mesoscale eddies. Therefore, we obtain the solution of the present model as the

wind-driven circulation inside the PV-homogenized region and the buoyancy-driven circulation outside the region.

## b. Parameters


Model parameters are chosen as suitable for the subtropical North Pacific ([Table 1](#) ). The model domain is a rectangular box extending from 15° to 45°N meridionally and 80° in zonal width. The Ekman pumping velocity,  $w_e$ , at the model surface is given as

$$w_e = -\frac{1}{\rho_0 f} \left( \frac{\partial \tau^x}{\partial y} \right), \quad (7)$$

$$\tau^x = -A \cos \frac{\pi(\theta - \theta_S)}{\theta_N - \theta_S}, \quad (8)$$

where  $\tau^x$  is the zonal wind stress;  $\theta$  is the latitude,  $\theta_S$  and  $\theta_N$  are its values at the southern and northern boundaries, and  $A$  is the amplitude of the wind stress, which is set as  $0.1 \text{ N m}^{-2}$ .

The interface densities are chosen as follows. The density distribution at the model surface, that is, at the upper interface of the surface layer, is given by a linear interpolation from  $22.5 \sigma_\theta$  at 15°N to  $25.5 \sigma_\theta$  at 45°N. The density at the interface between the surface and upper intermediate layers is chosen as  $26.5 \sigma_\theta$ . The  $26.5\text{-}\sigma_\theta$  surface is the densest isopycnal surface outcropping to relatively broad regions in the open ocean of the North Pacific in winter ([Keffer 1985](#); [Talley 1991](#)). Therefore, most waters denser than  $26.5 \sigma_\theta$  are not exposed to the direct wind forcings.

The next interface, which divides the middepth ocean into the upper and lower intermediate layers, is determined from isopycnal distributions of oxygen since different distributions of oxygen on isopycnal surfaces are caused by different flow patterns (e.g., [Reid 1965](#), [1997](#)). Above the surface of  $27.2 \sigma_\theta$  (e.g., Fig. 20 in [Reid 1965](#)), high oxygen concentration is found in the northwest of the North Pacific, where isopycnal surfaces lie at shallow depths, decreasing its concentration downstream around an anticyclonic gyre in the subtropics. On the other hand, below the  $27.2\text{-}\sigma_\theta$  surface (e.g., Fig. 25 in [Reid 1965](#); see also [Fig. 8](#) ), an oxygen-minimum water extends along 30°N, carried by the westward flow of the contracted anticyclonic gyre. South of this oxygen-minimum water, there is a tongue of high oxygen from the western boundary, originating from Antarctic Intermediate Water (AAIW). Therefore, we choose the interface density between the upper and lower intermediate layers as  $27.2 \sigma_\theta$ .

The bottom interface of the middepth ocean is defined as the density surface below which the PV-homogenized region does not exist. Below the depth of about 2000 m, the PV-homogenized region disappears and zonally oriented PV contours occupy the entire basin ([Talley 1988](#)). Therefore, the density surface of  $27.67 \sigma_\theta$  lying near the 2000-m depth is chosen as the lower interface of the lower intermediate layer.

The densities of the first three layers are given as  $25.25$ ,  $26.85$ , and  $27.44 \sigma_\theta$ , respectively. These values are the average values of the densities at the upper and lower interfaces. The density of the fourth layer is chosen as  $27.73 \sigma_\theta$ , which is roughly the average density of North Pacific Deep Water (NPDW: [Mantyla 1975](#)).

The layer thicknesses at the eastern boundary are set as  $H_1 = 300 \text{ m}$ ,  $H_2 = 500 \text{ m}$ , and  $H_3 = 900 \text{ m}$ , respectively. These values agree well with the values derived from a density distribution calculated from climatological data ([Levitus et al. 1994](#); [Levitus and Boyer 1994b](#)) along a 120°W meridional section near the eastern boundary in the North Pacific.

We choose the diapycnal diffusion coefficient as a constant value of  $5 \times 10^{-5} \text{ m}^2 \text{ s}^{-1}$ . Diapycnal diffusion coefficients estimated from microstructure observations below the thermocline are of the order  $10^{-5}$  to  $10^{-4} \text{ m}^2 \text{ s}^{-1}$  ([Toole et al. 1994](#)). The diapycnal velocity from the deep layer is assumed constant as  $w_3^* = 8.2 \times 10^{-8} \text{ m s}^{-1}$ . This value is obtained from [\(2\)](#), assuming the upper and lower interfaces of NPDW as the  $27.67\text{-}\sigma_\theta$  surface at 1700 m ( $H_1 + H_2 + H_3$ ) and the  $27.78\text{-}\sigma_\theta$  surface at 4000 m, respectively. The depth of 4000 m, at which the lower interface of NPDW lies, is selected from the analysis of water properties described by [Mantyla \(1975\)](#).

### 3. Results

#### a. Circulation in the model


Velocity fields in the upper and lower intermediate layers obtained from the model are shown in [Figs. 4a and 4b](#), respectively. The curve R2 (R3) represents the southern boundary of the PV-homogenized region in the upper (lower) intermediate layer. Outside the PV-homogenized region, although the PY model showed a zero velocity field, there are significant currents of the buoyancy-driven circulation in the present model. In the upper intermediate layer, a westward flow extends continuously to the south of an anticyclonic gyre within the PV-homogenized region. This circulation pattern is consistent with observed geostrophic flow fields at 500 db (e.g., [Reid 1997](#)).



In the lower intermediate layer, the PV-homogenized region, which is occupied by an anticyclonic gyre, contracts toward the northwestern corner of the model domain as shown in the PY model. Outside the PV-homogenized region, there is an eastward flow roughly south of the R2 curve. The velocity of the eastward flow has its meridional maxima along the R2 curve. The current speed there is as fast as that of the anticyclonic gyre flow in the PV-homogenized region. In addition to this prominent eastward flow, a westward flow appears just south of the PV-homogenized region. The maximum eastward flow along the R2 curve in the model is consistent with the eastward geostrophic flow observed around 20°N at 1000 db in the North Pacific ([Reid and Mantyla 1978](#); [Reid 1997](#)). The prominent eastward flow around 20°N has not been reproduced in previous models, which do not take account of the PV homogenization and diapycnal flows at the same time. The realistic reproduction of the eastward flow in the present model urges us to investigate further how the wind and buoyancy forcings work to yield this flow.


In order to understand the mechanism of the currents outside the PV-homogenized region, we examine the difference of diapycnal velocities between the upper and lower interfaces of each layer since the divergence of diapycnal velocity causes horizontal motion there as shown in (3). [Figures 5a and 5b](#) show the differences of diapycnal velocities,  $w_1^* - w_2^*$  and  $w_2^* - w_3^*$ , for the upper and lower intermediate layers, respectively. The diapycnal velocity diverges in the upper intermediate layer roughly south of the R2 curve with the magnitude of diapycnal divergence decreasing with latitude, while the diapycnal divergence in the lower intermediate layer is characterized by meridional maxima along the R2 curve. Because the horizontal variation of diapycnal velocity is larger at the upper interface than the lower one, the horizontal distribution of diapycnal divergence shown in [Fig. 5a](#) (b) is mainly characterized by the diapycnal velocity at the upper interface, namely,  $w_1^*$  ( $w_2^*$ ) for the upper (lower) intermediate layer. As shown in (2), the magnitude of diapycnal velocity depends on the layer thicknesses and the interface density differences. The northward decrease of  $w_1^*$  ([Fig. 5a](#)) is mainly a consequence of the northward increase of given surface density, that is, the resultant northward decrease of the interface density difference in the surface layer. However, the distribution of  $w_2^*$  ([Fig. 5b](#)) is controlled by the layer thicknesses with given constant interface densities.

At the position of R2, where the magnitude of  $w_2^*$  is meridionally maximal, the thickness of the upper (lower) intermediate layer,  $h_2^w$  ( $h_3^w$ ), is the smallest (largest) in the meridional direction as shown in [Fig. 2b](#). Both the minimum of  $h_2^w$  and the maximum of  $h_3^w$  contribute to the maximum of  $w_2^*$ , according to (2), and the occurrences of these minimum and maximum thicknesses are explained as follows. North of R2,  $h_2^w$  increases northward because of the assumption of uniform PV in the upper intermediate layer. On the other hand, south of R2,  $h_2^w$  increases southward because westward currents in the surface layer are associated with the southward decrease of  $h_1^w$ , while  $h_1^w + h_2^w$  is constant. At the same time, the wind-driven circulation within the PV-homogenized region in the upper intermediate layer yields the northward decrease of  $h_3^w$  from R2 to R3. Consequently, the wind-driven circulations in the surface layer and the upper intermediate layer within the PV-homogenized region characterize the distribution of diapycnal divergence in the lower intermediate layer, in which the meridional maxima of the divergence appear along the R2 curve.

The integration of diapycnal divergence along PV contours from the eastern boundary gives the solution of the PV equation, (3). We show the PV contours in the upper and lower intermediate layers in [Figs. 6a and 6b](#), respectively, superimposed upon the distribution of diapycnal divergence in each layer shown in [Fig. 5](#). The zonal velocity of the buoyancy-driven circulation is derived from the meridional difference in the integrated diapycnal divergence between neighboring PV contours. In the upper intermediate layer, the PV contours pass through the divergence field of diapycnal velocity with the magnitude of divergence decreasing toward the north. In this case, the zonal currents are generally westward as shown in [Fig. 4a](#). The same situation occurs in the region between the R2 and R3 curves in the lower intermediate layer. On the other hand, south of the R2 curve in the lower intermediate layer, the increase of diapycnal

divergence with increasing latitude gives rise to eastward flows in [Fig. 4b](#) .


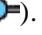
The reason why the eastward flows in the lower intermediate layer are strong only south of the R2 curve and currents are weak north of the curve can be explained in terms of the right-hand side of [\(5\)](#). The right-hand side is the product of the square of PV and the difference of diapycnal velocities. [Figure 6b](#)  indicates that south of the R2 curve both the PV and the difference of diapycnal velocities increase with increasing latitude, while north of the R2 curve the PV also increases, but the difference of diapycnal velocities decreases toward the north. Therefore, the meridional gradients of the right-hand side of [\(5\)](#) are larger on the southern side of the R2 curve than on the northern side, resulting in larger meridional gradients of  $d_3^t$  south of the R2 curve than the north via the integration of the right-hand side along PV contours. Consequently, the steeper (gentler)  $d_3^t$  gradients south (north) of the R2 curve cause strong (weak) flows there. Furthermore, as shown in [Fig. 5b](#) , the largest northward increase of the difference of diapycnal velocities appears just south of the R2 curve, resulting in a maximum eastward flow along the curve.



The maximum eastward flow is approximately parallel to the R2 curve, crossing PV contours toward the north. The velocity normal to a PV contour can be easily given by the local Sverdrup balance, [\(6\)](#), based on the distributions of diapycnal divergence and PV. Because the diapycnal velocity diverges in both the upper and lower intermediate layers outside the PV-homogenized regions, the normal velocities are approximately directed to the north. Near the PV-homogenized regions, however, the velocity fields shown in [Fig. 4](#)  exhibit a southward velocity component. This southward component is attributed to the velocity parallel to PV contours, which has to be taken into account the integration of remote diapycnal divergence along the PV contours. The meridional component of the parallel velocity dominates over that of the normal velocity near the PV-homogenized region because the PV contours tilt meridionally, resulting in southward motion there.

### *b. Circulation in the North Pacific*

In the previous subsection, we have shown that the buoyancy forcing associated with the density structure resulting from the wind-driven circulation causes currents outside the PV-homogenized region. In the present subsection, we will describe the consistency of the model circulation in terms of a current field obtained diagnostically from the observed density structure in the North Pacific, and the distribution of dissolved oxygen there.

In order to estimate the diagnostic current field in the North Pacific, we calculated a climatological annual-mean density field from climatological temperature data ([Levitus and Boyer 1994b](#)) and salinity data ([Levitus et al. 1994](#)). Our viewpoint is directed to the circulation in the lower intermediate layer of the North Pacific because an interesting eastward flow outside the PV-homogenized region was predicted in the present analytical model. Recent float observations in the western North Pacific ([Riser 1995](#)) indicated that the velocity of the eastward flow around 20°N at the depth of 1000 m is the order 0.01 m s<sup>-1</sup> (1 cm s<sup>-1</sup>). To compare with this observed velocity at the 1000-m depth, we will show the average velocity in a layer between the surfaces of 27.2 and 27.5  $\sigma_\theta$ , the depths of which are about 800 and 1200 m, respectively, around 20°N. We have chosen this layer instead of the lower intermediate layer itself (27.2–27.67  $\sigma_\theta$ , and 800–2000 m around 20°N) because we need to choose a layer with the density surfaces near the float observation depth (1000 m) for a quantitative comparison. The magnitude of diagnosed velocity averaged in a layer depends on its vertical levels; the resultant flow pattern for the layer of 27.2–27.67  $\sigma_\theta$  is qualitatively similar to that for the layer of 27.2–27.5  $\sigma_\theta$ , but the velocity magnitude of the former layer is about a half of the latter layer (not shown).

Based on the climatological density distribution, we can obtain the thickness distribution of the layer defined above with the interface densities of 27.2 and 27.5  $\sigma_\theta$ . Then, the distribution of PV, Coriolis parameter divided by the layer thickness, is given in [Fig. 7a](#) . The PV distribution is characterized by a homogenized region north of 30°N, and a steep meridional gradient region south of the homogenized region. These features have also found in the analytical model (see [Fig. 6b](#) .

From the advective–diffusive equation of [\(1\)](#) applying to the climatological density field, we can calculate the diapycnal velocities at the top and bottom of the layer of 27.2–27.5  $\sigma_\theta$ . The density surfaces of 26.5 (27.2), 27.2 (27.5), and 27.5 (27.78)  $\sigma_\theta$  are used to estimate the diapycnal velocity at the 27.2 (27.5)  $\sigma_\theta$  surface. These density surfaces are the boundaries of the layers which were described in [section 2b](#) except for the 27.5- $\sigma_\theta$  surface, which was defined above. We show the difference of diapycnal velocities between the top and bottom of the layer of 27.2–27.5  $\sigma_\theta$  in [Fig. 7b](#) . In this estimation, we used a diffusion coefficient of  $0.5 \times 10^{-4}$  m<sup>2</sup> s<sup>-1</sup> as in the analytical model. The maximum divergence of diapycnal velocity in the meridional direction occurs along 15°–20°N. Again, this feature is common to the divergence field in the analytical model shown in [Fig. 5b](#) .

When the buoyancy forcing, which is caused by the divergence of diapycnal velocity shown in [Fig. 7b](#), is integrated along PV contours emanating from the eastern boundary ([Fig. 7a](#)), the pressure field and hence the velocity field of geostrophic motion in the layer of  $27.2\text{--}27.5\ \sigma_\theta$  are obtained. [Figure 7c](#) shows the velocity field, which is a result of a three-point median smoothing ([Rabiner et al. 1975](#)) to remove extraordinary large velocity vectors. As in the analytical model, the velocity in the PV-homogenized region, where the PV contours from the eastern boundary do not penetrate, is not obtained. It is noteworthy that in this estimation we do not have to distinguish how the distribution of density surfaces (layer thicknesses) is determined by the wind and buoyancy forcings, though in the analytical model treated above we have assumed that the distribution of density surfaces (layer thicknesses) is characterized by the wind-driven circulation. This assumption is removed in the present diagnostic estimation by using the observed density field.

The circulation pattern shown in [Fig. 7c](#) is remarkably similar to that in [Fig. 4b](#). The meridional maxima of eastward currents in [Fig. 7c](#) appear along the zone where the divergence of diapycnal velocity is meridionally maximal in [Fig. 7b](#). The velocity of the maximum eastward flow is, however, of the order  $0.005\ \text{m s}^{-1}$  ( $0.5\ \text{cm s}^{-1}$ ), which is a half of that obtained from float observations ([Riser 1995](#)). The diapycnal diffusion coefficient of  $0.5 \times 10^{-4}\ \text{m}^2\ \text{s}^{-1}$  used in the present diagnostics, which has been chosen to be a midvalue of observational uncertainties from  $1 \times 10^{-5}$  to  $1 \times 10^{-4}\ \text{m}^2\ \text{s}^{-1}$  ([Toole et al. 1994](#)), might be underestimated. If we employed an upper bound of the observational uncertainties, the resultant magnitude of diagnosed velocity would be as large as the observed one. The use of a larger diffusion coefficient is supported from a numerical investigation by [Tsujino et al. \(2000\)](#), who suggested that a relatively large value of  $1 \times 10^{-4}\ \text{m}^2\ \text{s}^{-1}$  at the lower thermocline depth ( $\sim 1000\ \text{m}$ ) is necessary for the reproduction of a realistic deep-Pacific meridional transport.

We further examine whether the circulation in [Fig. 7c](#) is consistent with the oxygen distribution in the North Pacific. [Figure 8](#) shows the climatological annual-mean oxygen distribution ([Levitus and Boyer 1994a](#)) on the density surface of  $27.4\ \sigma_\theta$ , which is a representative level for the oxygen distribution in the lower intermediate layer. The distribution pattern indicates that a tongue of oxygen-rich water extends from the western boundary into the ocean interior around  $20^\circ\text{N}$ . This oxygen-rich tongue was interpreted as an evidence of the eastward flow obtained from a geostrophic calculation at the 1000-db level ([Reid and Mantyla 1978](#)). The latitudes of the oxygen-rich tongue strikingly coincide with the latitudes of the meridional maxima of the eastward velocity estimated diagnostically from the observed density field (cf. [Fig. 7c](#) and [Fig. 8](#)). This agreement of the latitudes qualitatively supports the validity of the present estimation. If other forcings, such as eddy activities, were more important than the diapycnal divergence, the zone of the oxygen-rich tongue would not necessarily coincide with the core of the diagnosed eastward flow. The agreement, furthermore, indicates that the circulation driven by the diapycnal divergence plays an important role in the water-property distributions outside the PV-homogenized region in the lower intermediate layer of the North Pacific.


#### 4. Discussion

We have proposed a model, which takes both wind and buoyancy forcings into account, on the middepth water circulation, and have applied this model to the subtropical North Pacific. The applicability of the present analytical model depends on whether the wind-driven model based on the theories of PV homogenization successfully reproduces the observed PV and density stratification. In this case, we can obtain an analytical solution on the buoyancy-driven circulation under the background stratification specified by the wind-driven circulation. As described in [section 1](#), the stratification in the subtropical North Pacific is well reproduced by the wind-driven model of PV homogenization. On the other hand, the present analytical model cannot be applied to oceans whose stratification is not well approximated to that obtained solely from the wind-driven model and significantly influenced by thermohaline effects such as deep convection due to surface cooling and its associated basin-scale circulation. For example, in the North Atlantic, a well-developed PV-homogenized region is not observed ([Keffer 1985](#)), and the stratification above the deep water (North Atlantic Deep Water) cannot be explained by the PV-homogenization model. In this region, PV contours incline to a north–south direction to intersect the subtropical–subpolar gyre boundary, suggesting northward motion there due to the combined effects of Ekman suction and deep convection at high latitudes ([Keffer 1985](#)). The interaction between wind and thermohaline effects is likely to be stronger in the North Atlantic than in the North Pacific. To investigate the combined influence of wind and thermohaline forcings in the North Atlantic, probably we need to employ numerical models. A numerical model studied by [Huang and Bryan \(1987\)](#) successfully explained the circulation and PV distribution in the North Atlantic.

Likewise, in the North Pacific, numerical models are potentially useful tools for the investigations of the combined influence of wind and thermohaline forcings. However, limited computer resources available today do not allow us to examine the combined forcings adequately. For the reproduction of the middepth water circulation driven by the combined forcings, such as the buoyancy-driven circulation treated in the present study, one needs to reproduce the PV-homogenized region in a numerical model first. Because the PV-homogenized region results from eddy processes, a numerical model that successfully reproduces the PV-homogenized region must properly resolve the eddy processes with a fine grid spacing. On the other hand, in order to establish a thermohaline balance in the ocean, the integration time must be as long as the order of



the resident time of water. In other words, the model must be integrated for hundreds of years. Three-dimensional primitive-equation models have not yet satisfied those two requirements, namely, high resolution with a long integration time at the same time. There have been numerical studies with low resolution and a long integration time (e.g., [England 1993](#); [Ishizaki 1994](#); [Tsujino and Sugimoto 1998, 1999](#); [Yamanaka et al. 1998](#)), or with high resolution (finer than  $1^\circ \times 1^\circ$ ) and a relatively short integration time of the order of a few decades (e.g., [Semtner and Chervin 1988, 1992](#); [Hurlburt et al. 1996](#)). Although these two requirements are rather easily satisfied by using quasi-geostrophic models, these models did not take account of the diapycnal flows through interfaces between layers (e.g., [Holland and Rhines 1980](#); [Holland et al. 1984](#); [Lozier and Riser 1989](#)).

Even with low resolution ( $1^\circ$  lat  $\times$   $2^\circ$  long), a general circulation model (GCM) studied by Yamanaka et al. (1988) gives us some information about the middepth water circulation in the North Pacific. The GCM exhibits an eastward flow at the 1000-m depth along  $10^\circ$ – $15^\circ$ N. The eastward flow, however, shifts southward about five degrees in its latitude compared with the diagnosed eastward flow corresponding to the high-oxygen tongue in our estimation. Although [Yamanaka et al. \(1998\)](#) did not mention the mechanism of the eastward flow, the similarity between the results of the GCM and the present study suggests the importance of further analyses of the GCM results from the viewpoint of the combined influence of wind and buoyancy forcings. The southward shift of the eastward flow might be related to a southward extension of concave density surfaces, which represent the existence of an anticyclonic gyre, below the  $27.2\text{-}\sigma_\theta$  surface in the GCM (See Fig. 10a in [Yamanaka et al. 1998](#)) in comparison with the climatological density structure (Fig. 2a ). The southward extension of concave density surfaces in the GCM might be due to insufficient resolution to resolve eddy processes which play an important role in characterizing density stratification.

Interestingly, using a GCM, [Tsujino and Sugimoto \(1999\)](#) proposed a mechanism of combined wind and buoyancy forcings working on circulations. They showed that a subpolar wind-driven circulation intensifies a basin-scale thermohaline circulation. The intensification is attributed to enhanced surface heating due to stratification strengthened by Ekman upwelling in the subpolar circulation. They called this thermohaline circulation the *wind-enhanced thermohaline circulation*. For the wind-enhanced thermohaline circulation, most of the PV input caused by the buoyancy forcing is likely to occur in the subpolar ocean, but for the buoyancy-driven circulation in the present study, the PV input occurs in the subtropical ocean. Consequently, these two types of the combined wind and buoyancy forcings play roles in different regions of the ocean, and can coexist in the ocean.

In addition to the buoyancy-driven circulation, other mechanisms might contribute to the middepth water circulation in the North Pacific. The conceivable other mechanisms are of the flows induced by eddy activities, cross-gyre flows connecting subpolar and subtropical gyres, and steady flows driven by time-varying wind or buoyancy forcings. As described in [section 1](#), the PV input associated with eddy activities is not likely to produce a significant flow away from the PV-homogenized region.

Cross-gyre flows were theoretically studied by using pure wind-driven models (e.g., [Chen and Dewar 1993](#)), or a wind-driven model with a prescribed buoyancy forcing at the gyre boundary ([Luyten and Stommel 1986a](#)). In this context, the wind-enhanced thermohaline circulation proposed by [Tsujino and Sugimoto \(1999\)](#) and its circulation in the North Pacific ([Tsujino and Sugimoto 1998](#)) also form a cross-gyre flow, which is mainly driven by buoyancy forcing interacting with the subpolar wind-driven circulation. In the present model, we treated only the subtropical ocean, and the wind-driven circulation was prescribed not to have a cross-gyre component, and hence the cross-gyre flows of [Tsujino and Sugimoto \(1998, 1999\)](#) and [Chen and Dewar \(1993\)](#) were not taken into account. However, because the cross-gyre flows approximately conserve PV in the interior of the ocean, the flows are almost parallel to PV contours, passing the gyre boundary through a *window* where the meridional gradient of PV is quite small. In the middepth ocean, such a window at the gyre boundary is restricted to inside or just east of the PV-homogenized region, and hence the cross-gyre flows do not locate away from the homogenized region.

Time-varying wind or buoyancy forcings may cause steady currents in the middepth ocean. [Liu \(1993a,b\)](#) suggested that time-varying wind stresses produce a westward flow just south of a wind-driven gyre that is caused by the time-mean wind stresses because strong variability of stratification due to the time-varying forcings occurs there. Furthermore, [Liu and Pedlosky \(1994\)](#) showed that time-varying buoyancy forcings at the sea surface can significantly influence the steady flow field in the ventilated thermocline through subducted waters, while this influence is insignificant outside the ventilated zone.

Consequently, several possible mechanisms produce water movements in the middepth ocean of the North Pacific, but each mechanism causes a flow in a specific region. Among those mechanisms, only the PV input associated with the buoyancy forcing controlled by the wind-driven circulation can produce a significant flow away from the PV-homogenized region. Therefore, the combined influence of wind and buoyancy forcings presented in this study is the most plausible mechanism that produces an eastward flow around  $20^\circ$ N in the lower intermediate layer observed from hydrographic measurements (e.g., [Reid 1997](#)) and float drift ([Riser 1995](#)).

## 5. Conclusions

In the present paper, we have proposed a model in which both wind and buoyancy forcings are taken into account in the middepth water circulation. A similar combination of these forcings was analytically studied by [Tziperman \(1986\)](#) for a buoyancy-driven circulation controlled by the ventilated-thermocline circulation. We focused, however, on the controlled influence by the PV homogenization, which is a mechanism of the unventilated wind-driven circulation, for buoyancy-driven circulations in the upper and lower intermediate layers. The buoyancy forcing is caused by the divergence of diapycnal flow, which was assumed to be in a steady diapycnal advective–diffusive density balance. Because the PV-homogenization theories of RY82a,b and PY explained successfully the density distribution in the North Pacific, in which well developed PV-homogenized regions were observed, we have safely assumed that the diapycnal advection is constrained by the density distribution associated with the wind-driven circulation. In other words, the distribution of the buoyancy forcing is controlled by the wind-driven circulation. Then the flow field resulting from the buoyancy forcing can be obtained analytically, and the total flow field is given by the sum of the wind-driven circulation and buoyancy-driven circulation.

The resultant velocity field exhibited a westward flow south of the PV-homogenized region in the upper intermediate layer while, more interestingly, in the lower intermediate layer a prominent eastward flow appeared along the southern rim of the PV-homogenized region in the upper intermediate layer due to the maximum diapycnal divergence there. The presence of the eastward flow in the lower intermediate layer was supported by a diagnosed velocity field obtained from the observed density field in the North Pacific. Furthermore, the diagnosed location of the prominent eastward flow strikingly coincided with the position of the eastward-extending tongue of high-oxygen water around 20°N. In this region away from the PV-homogenized region, only the buoyancy forcing is likely to cause a significant flow, though several mechanisms might contribute to drive flows inside or near the PV-homogenized region. The buoyancy-driven circulation, which is controlled by the wind-driven circulation, is most likely to play an important role in the oceanic circulation away from the PV-homogenized region and the water-property distributions in the middepth ocean of the North Pacific.

### Acknowledgments

The authors would like to express their sincere thanks to Professor Seiichi Kanari for fruitful discussions and invaluable suggestions. They also acknowledge Dr. Hiroyasu Hasumi, Dr. Toshiyuki Hibiya, Dr. Atsushi Kubokawa, Dr. Hirohiko Nakamura, and Dr. Yasuhiro Yamanaka for their fruitful comments, and Dr. Hiroyuki Tsujino for reprints and preprints. This study benefited from discussions with Dr. Julian P. McCreary and Dr. Stephen C. Riser. Thanks also go to reviewers who helped improve this manuscript. The present paper is part of a doctoral thesis (S. Nishino) submitted to Hokkaido University.

---

### REFERENCES

- Chen, L. G., and W. K. Dewar, 1993: Intergyre communication in a three-layer model. *J. Phys. Oceanogr.*, **23**, 855–878.
- Cushman-Roisin, B., 1987: On the role of heat flux in the Gulf Stream–Sargasso Sea subtropical gyre system. *J. Phys. Oceanogr.*, **17**, 2189–2202.
- de Szoeke, R. A., 1995: A model of wind- and buoyancy-driven ocean circulation. *J. Phys. Oceanogr.*, **25**, 918–941.
- England, M. H., 1993: Representing the global-scale water masses in ocean general circulation models. *J. Phys. Oceanogr.*, **23**, 1523–1552.
- Holland, W. R., and P. B. Rhines, 1980: An example of eddy induced circulation. *J. Phys. Oceanogr.*, **10**, 1010–1031.
- , T. Keffer, and P. B. Rhines, 1984: Dynamics of the ocean general circulation. *Nature*, **308**, 698–705.
- Huang, R. X., and K. Bryan, 1987: A multilayer model of the thermohaline and wind-driven ocean circulation. *J. Phys. Oceanogr.*, **17**, 1909–1924.
- Hurlburt, H. E., A. J. Wallcraft, W. J. Schmitz Jr., P. J. Hogan, and E. J. Metzger, 1996: Dynamics of the Kuroshio/Oyashio current system using eddy-resolving models of the North Pacific Ocean. *J. Geophys. Res.*, **101**, 941–976.
- Ishizaki, H., 1994: A simulation of the abyssal circulation in the North Pacific Ocean. Part I: Flow field and comparison with observations. *J. Phys. Oceanogr.*, **24**, 1921–1939.
- Keffer, T., 1985: The ventilation of the world’s oceans: Maps of the potential vorticity field. *J. Phys. Oceanogr.*, **15**, 509–523.
- Levitus, S., and T. P. Boyer, 1994a: *World Ocean Atlas 1994*. Vol 2: *Oxygen*. NOAA Atlas NESDIS 2, 186 pp.
- , and —, 1994b: *World Ocean Atlas 1994*. Vol. 4: *Temperature*. NOAA Atlas NESDIS 4, 117 pp.

— R. Burgett, and T. P. Boyer, 1994: *World Ocean Atlas 1994*, Vol. 3, *Salinity*. NOAA Atlas NESDIS 3, 99 pp.

Liu, Z., 1993a: Thermocline variability forced by varying Ekman pumping. Part I: Spinup and spindown. *J. Phys. Oceanogr.*, **23**, 2505–2522.

— 1993b: Thermocline variability forced by varying Ekman pumping. Part II: Annual and decadal Ekman pumping. *J. Phys. Oceanogr.*, **23**, 2523–2540.

— and J. Pedlosky, 1994: Thermocline forced by annual and decadal surface temperature variation. *J. Phys. Oceanogr.*, **24**, 587–608.

Lozier, M. S., and S. C. Riser, 1989: Potential vorticity dynamics of boundary currents in a quasigeostrophic ocean. *J. Phys. Oceanogr.*, **19**, 1373–1396.

Luyten, J. R., and H. Stommel, 1986a: Experiments with cross-gyre flow patterns on a beta-plane. *Deep-Sea Res.*, **33**, 963–972.

— and — 1986b: Gyres driven by combined wind and buoyancy flux. *J. Phys. Oceanogr.*, **16**, 1551–1560.

— J. Pedlosky, and H. Stommel, 1983: The ventilated thermocline. *J. Phys. Oceanogr.*, **13**, 292–309.

Mantyla, A. W., 1975: On the potential temperature in the abyssal Pacific Ocean. *J. Mar. Res.*, **33**, 341–354.

Munk, W. H., 1966: Abyssal recipes. *Deep-Sea Res.*, **13**, 707–730.

Pedlosky, J., 1986: The buoyancy and wind-driven ventilated thermocline. *J. Phys. Oceanogr.*, **16**, 1077–1087.

— and W. R. Young, 1983: Ventilation, potential vorticity homogenization and the structure of the ocean circulation. *J. Phys. Oceanogr.*, **13**, 2020–2037.

Rabiner, L. R., M. R. Sambur, and C. E. Schmidt, 1975: Application of a nonlinear smoothing algorithm to speech processing. *IEEE Trans. on Acoustic, Speech and Signal Processing*, **ASSP-23**, 552–557.

Reid, J. L., Jr., 1965: Intermediate waters of the Pacific Ocean. *Johns Hopkins Oceanogr. Stud.*, No. 2, 1–85.

— 1997: On the total geostrophic circulation of the Pacific Ocean: flow patterns, tracers, and transports. *Progress in Oceanography*, Vol. 39, Pergamon, 263–352.

— and R. S. Arthur, 1975: Interpretation of maps of geopotential anomaly for the deep Pacific Ocean. *J. Mar. Res.*, **33**(Suppl.), 37–52.

— and A. W. Mantyla, 1978: On the mid-depth circulation of the North Pacific Ocean. *J. Phys. Oceanogr.*, **8**, 946–951.

Rhines, P. B., and W. R. Young, 1982a: A theory of the wind-driven circulation. I. Mid-ocean gyres. *J. Mar. Res.*, **40**(Suppl), 559–596.

— and — 1982b: Homogenization of potential vorticity in planetary gyres. *J. Fluid Mech.*, **122**, 347–367.

Riser, S. C., 1995: Pacific RAFOS floats measure mid-depth flow. *WOCE Notes*, **7**, 1–6.

Schmitz, W. J., Jr., and W. R. Holland, 1982: A preliminary comparison of selected numerical eddy-resolving general circulation experiments with observations. *J. Mar. Res.*, **40**, 75–117.

— and — 1986: Observed and modeled mesoscale variability near the Gulf Stream and Kuroshio Extension. *J. Geophys. Res.*, **91**, 9624–9638.

Semtner, A. J., Jr., and R. M. Chervin, 1988: A simulation of the global ocean circulation with resolving eddies. *J. Geophys. Res.*, **93**, 15502–15522.

— and — 1992: Ocean general circulation from a global eddy-resolving model. *J. Geophys. Res.*, **97**, 5493–5550.

Stommel, H., and A. B. Arons, 1960a: On the abyssal circulation of the world ocean-I. Stationary planetary flow patterns on a sphere. *Deep-Sea Res.*, **6**, 140–154.

— and — 1960b: On the abyssal circulation of the world ocean-II. An idealized model of the circulation pattern and amplitude in oceanic basins. *Deep-Sea Res.*, **6**, 217–233.

Talley, L. D., 1988: Potential vorticity distribution in the North Pacific. *J. Phys. Oceanogr.*, **18**, 89–106.

— 1991: An Okhotsk Sea water anomaly: Implications for ventilation in the North Pacific. *Deep-Sea Res.*, **38**, S171–S190.

Toole, J. M., K. L. Polzin, and R. W. Schmitt, 1994: Estimations of diapycnal mixing in the abyssal ocean. *Science*, **264**, 1120–1123.

Tsujino, H., and N. Suginohara, 1998: Thermohaline effects on upper layer circulation of the North Pacific. *J. Geophys. Res.*, **103**, 18665–18679.

—, and —, 1999: Thermohaline circulation enhanced by wind forcing. *J. Phys. Oceanogr.*, **29**, 1506–1516.

—, H. Hasumi, and N. Suginohara, 2000: Deep Pacific circulation controlled by vertical diffusivity at the lower thermocline depths. *J. Phys. Oceanogr.*, in press.

Tziperman, E., 1986: On the role of interior mixing and air–sea fluxes in determining the stratification and circulation of the ocean. *J. Phys. Oceanogr.*, **16**, 680–693.

Veronis, G., 1978: Model of world ocean circulation: III. Thermally and wind driven. *J. Mar. Res.*, **36**, 1–44.

Yamanaka, G., Y. Kitamura, and M. Endoh, 1998: Formation of North Pacific Intermediate Water in Meteorological Research Institute ocean general circulation model. 1. Subgrid-scale mixing and marginal sea fresh water. *J. Geophys. Res.*, **103**, 30885–30903.

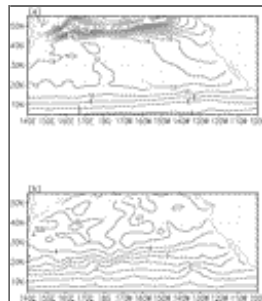
## Tables

Table 1. Parameter values used in the model

Parameter	Value
Latitudinal extent	15°–45°N
Longitudinal width	80°
Amplitude of wind stress ( $\tau$ )	0.1 N m <sup>-2</sup>
Density	
Surface layer ( $\rho_s$ )	25.25 $\sigma_\theta$
Upper intermediate layer ( $\rho_u$ )	26.85 $\sigma_\theta$
Lower intermediate layer ( $\rho_l$ )	27.45 $\sigma_\theta$
Deep layer ( $\rho_d$ )	27.73 $\sigma_\theta$
Interface density	
Model surface ( $\rho_1^*$ )	25.5 $\sigma_\theta$ (15°N)–25.5 $\sigma_\theta$ (45°N)
Surface–upper intermediate layers ( $\rho_2^*$ or $\rho_3^*$ )	26.5 $\sigma_\theta$
Upper–lower intermediate layers ( $\rho_4^*$ or $\rho_5^*$ )	27.2 $\sigma_\theta$
Lower intermediate–deep layers ( $\rho_6^*$ )	27.67 $\sigma_\theta$
Layer thickness at the eastern boundary	
Surface layer ( $H_s$ )	300 m
Upper intermediate layer ( $H_u$ )	200 m
Lower intermediate layer ( $H_l$ )	900 m
Diapycnal diffusion coefficient ( $\kappa_v$ )	$5 \times 10^{-11}$ m <sup>2</sup> s <sup>-1</sup>
Diapycnal velocity from the deep layer ( $v_v$ )	$8.2 \times 10^{-6}$ m s <sup>-1</sup>

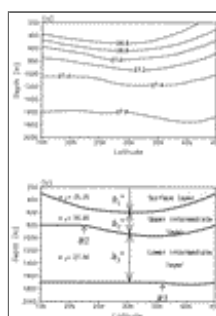
[Click on thumbnail for full-sized image.](#)

## Figures



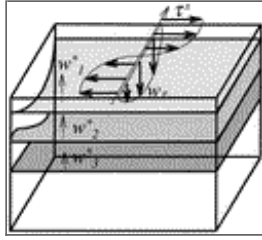
[Click on thumbnail for full-sized image.](#)

Fig. 1. Distributions of potential vorticity in the North Pacific along isopycnal surfaces of (a) 26.8 and (b) 27.4  $\sigma_\theta$ . Values of potential vorticity are calculated as  $-\rho^{-1}f\partial\rho/\partial z$ , where  $\rho$  is density and  $f$  is the Coriolis parameter. The density field is obtained from climatological data of temperature (Levitus and Boyer 1994b) and salinity (Levitus et al. 1994). Units of the contour labels are  $10^{-11} \text{ m}^{-1} \text{ s}^{-1}$ , and the contour intervals are  $2 \times 10^{-11}$  and  $0.5 \times 10^{-11} \text{ m}^{-1} \text{ s}^{-1}$  for (a) and (b), respectively



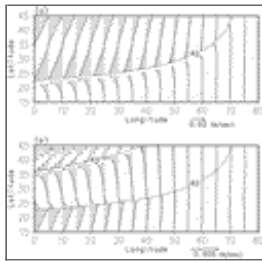
[Click on thumbnail for full-sized image.](#)

Fig. 2. Meridional cross sections of (a) observed density surfaces along the date line, and (b) modeled layer interfaces at a location equivalent to the date line. The distance from this location to the eastern boundary of the model is taken as  $80^\circ$ , which is approximately equivalent to the distance between the date line and the coast of North America. The observed density distribution is based on the climatological data of [Levitus et al. \(1994\)](#) and [Levitus and Boyer \(1994b\)](#). The model is similar to that proposed by [Pedlosky and Young \(1983\)](#), but ventilated layers in their model are simplified into one layer. Details of the model description are given in [section 2a](#), in terms of layer thicknesses of  $h_1^w$ ,  $h_2^w$ , and  $h_3^w$ . In (a), contours in the surface layer less than  $26.5 \sigma_\theta$  are omitted to avoid crowding. In (b), R2 (R3) represents the position of the southern boundary of the potential vorticity homogenized region in the upper (lower) intermediate layer



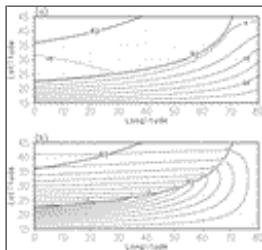
[Click on thumbnail for full-sized image.](#)

Fig. 3. Schematic representation of the  $3\frac{1}{2}$ -layer model. Ekman pumping,  $w_e$ , is given by the curl of wind stress,  $\tau^x$ . Diapycnal flows,  $w_1^*$ ,  $w_2^*$ , and  $w_3^*$ , are taken into account as the forcing accompanied by the thermohaline process of diapycnal advective–diffusive density balance



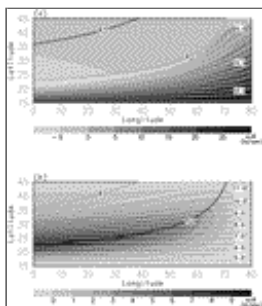
[Click on thumbnail for full-sized image.](#)

Fig. 4. Velocity fields obtained from the model in (a) the upper intermediate layer, and (b) the lower intermediate layer. In the region north of the curve R2 (R3), potential vorticity is homogenized in the upper (lower) intermediate layer



[Click on thumbnail for full-sized image.](#)

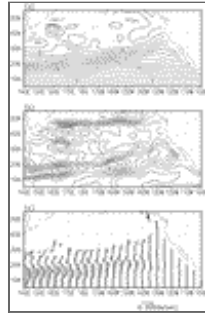
Fig. 5. Divergence fields of diapycnal velocity in (a) the upper intermediate layer and (b) the lower intermediate layer. Values in the fields are given as (a)  $w_1^* - w_2^*$  and (b)  $w_2^* - w_3^*$ . The units of the contour labels are  $10^{-8} \text{ m s}^{-1}$ , and the contour intervals are  $5 \times 10^{-8}$  and  $1 \times 10^{-8} \text{ m s}^{-1}$  for (a) and (b), respectively. The two curves, R2 and R3, are the same as those shown in [Fig. 4](#)



[Click on thumbnail for full-sized image.](#)

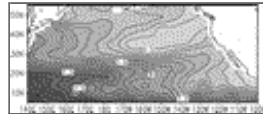
Fig. 6. Characteristic paths (white contours) and divergence fields of diapycnal velocity (shades) in (a) the upper intermediate

layer, and (b) the lower intermediate layer. The characteristic paths are given as curved or straight lines of  $f/h^w_2 = \text{const}$  and  $f/h^w_3 = \text{const}$  in the upper and lower intermediate layers, respectively. The units of the contour labels are  $10^{-8} \text{ m}^{-1} \text{ s}^{-1}$ , and the contour intervals are  $1 \times 10^{-8}$  and  $0.5 \times 10^{-8} \text{ m}^{-1} \text{ s}^{-1}$  for (a) and (b), respectively. The divergence fields of diapycnal velocity shown in [Fig. 5](#) are superimposed with shading. Darker (lighter) shades represent larger (smaller) divergence



[Click on thumbnail for full-sized image.](#)

Fig. 7. Distributions of (a) potential vorticity in the layer defined by the density surfaces of  $27.2$  and  $27.5 \sigma_\theta$  in the North Pacific, (b) the difference of diapycnal velocities between the upper and lower interfaces of the layer, and (c) current velocity averaged in the layer caused by the divergence of diapycnal velocity. In (a) values of potential vorticity are calculated by dividing the Coriolis parameter by the layer thickness. The units of the contour labels are  $10^{-8} \text{ m}^{-1} \text{ s}^{-1}$ , and the contour interval is  $1 \times 10^{-8} \text{ m}^{-1} \text{ s}^{-1}$ . The contours correspond to the characteristic paths to obtain the velocity field in (c). In (b) the units of the contour labels are  $10^{-8} \text{ m s}^{-1}$ , and the contour interval is  $1 \times 10^{-8} \text{ m s}^{-1}$ . In (c) the region where the velocity vectors are not shown is sheltered from the penetration of characteristic paths from the eastern boundary. Therefore, in this region, the solution of the currents cannot be obtained



[Click on thumbnail for full-sized image.](#)

Fig. 8. Concentration of dissolved oxygen ( $\text{ml L}^{-1}$ ) along the density surface of  $27.4 \sigma_\theta$ . The density surface lies within the lower intermediate layer ( $27.2\text{--}27.67 \sigma_\theta$ ) of the North Pacific

\* Current affiliation: Japan Marine Science and Technology Center, Yokosuka, Japan.

+ Additional affiliation: Frontier Research System for Global Change, Tokyo, Japan.

Corresponding author address: Dr. Shigeto Nishino, Ocean Research Department, Japan Marine Science and Technology Center, Yokosuka 237-0061, Japan.

E-mail: [nishinos@jamstec.go.jp](mailto:nishinos@jamstec.go.jp)

[top](#) ▲



© 2008 American Meteorological Society [Privacy Policy and Disclaimer](#)  
 Headquarters: 45 Beacon Street Boston, MA 02108-3693  
 DC Office: 1120 G Street, NW, Suite 800 Washington DC, 20005-3826  
[amsinfo@ametsoc.org](mailto:amsinfo@ametsoc.org) Phone: 617-227-2425 Fax: 617-742-8718  
[Allen Press, Inc.](#) assists in the online publication of AMS journals.